Muon flux measurement at China Jinping Underground Laboratory[*]

Zi-yi Guo(郭子溢)[1,2]   Lars Bathe-Peters[1,4]   Shao-min Chen(陈少敏)[1,2,3†]   Mourad Chouaki[1,5]   Wei Dou(窦威)[1,2]

Lei Guo(郭磊)[1,2]   Ghulam Hussain[1,2]   Jin-jing Li(李进京)[1,2]   Qian Liu(刘倩)[6]   Guang Luo(罗光)[7]

Wen-tai Luo(骆文泰)[6]   Ming Qi(祁鸣)[8]   Wen-hui Shao(邵文辉)[1,2]   Jian Tang(唐健)[7]   Lin-yan Wan(万林焱)[1,2]

Zhe Wang(王喆)[1,2,3]   Ben-da Xu(续本达)[1,2,3]   Tong Xu(徐彤)[1,2]   Wei-ran Xu(徐蔚然)[1,2]   Yu-zi Yang(杨玉梓)[1,2]

Minfang Yeh[9]   Lin Zhao(赵林)[1,2]

(JNE Collaboration)

[1]Department of Engineering Physics, Tsinghua University, Beijing 100084, China
[2]Center for High Energy Physics, Tsinghua University, Beijing 100084, China
[3]Key Laboratory of Particle & Radiation Imaging (Tsinghua University), Ministry of Education, China
[4]Institut für Physik, Technische Universität Berlin, Berlin 10623, Germany
[5]École Polytechnique Fédérale de Lausanne, Lausanne 1015, Switzerland
[6]School of Physical Sciences, University of Chinese Academy of Sciences, Beijing 100049, China
[7]School of Physics, Sun Yat-Sen University, Guangzhou 510275, China
[8]School of Physics, Nanjing University, Nanjing 210093, China
[9]Brookhaven National Laboratory, Upton, New York 11973, USA

Abstract: China Jinping Underground Laboratory (CJPL) is ideal for studying solar, geo-, and supernova neutrinos. A precise measurement of the cosmic-ray background is essential in proceeding with R&D research for these MeV-scale neutrino experiments. Using a 1-ton prototype detector for the Jinping Neutrino Experiment (JNE), we detected 264 high-energy muon events from a 645.2-day dataset from the first phase of CJPL (CJPL-I), reconstructed their directions, and measured the cosmic-ray muon flux to be $(3.53 \pm 0.22_{stat.} \pm 0.07_{sys.}) \times 10^{-10}$ cm^{-2}s^{-1}. The observed angular distributions indicate the leakage of cosmic-ray muon background and agree with simulation data accounting for Jinping mountain's terrain. A survey of muon fluxes at different laboratory locations, considering both those situated under mountains and those down mine shafts, indicates that the flux at the former is generally a factor of (4 ± 2) larger than at the latter, with the same vertical overburden. This study provides a convenient back-of-the-envelope estimation for the muon flux of an underground experiment.

Keywords: CJPL, cosmic-ray muon flux, angular distribution, neutrino detector, liquid scintillator

DOI: 10.1088/1674-1137/abccae

I. INTRODUCTION

The China Jinping Underground Laboratory (CJPL), located in Sichuan Province, China, is one of the world's deepest underground laboratories [1]. The rock overburden at CJPL is about 2400 m vertically [2] and the closest nuclear power plant is approximately 1000 km away. It is an ideal site for rare-event experiments such as dark matter searches [3, 4], neutrinoless double beta decay [5, 6], and solar neutrino studies. The proposed Jinping Neutrino Experiment aims to study MeV-scale low-energy neutrinos, including solar neutrinos, geoneutrinos, and supernova relic neutrinos (also referred to as the diffuse supernova neutrino background) [7-9].

These studies are very prone to contamination from cosmic-ray muons and muon-induced radioactive isotope backgrounds. From the dominant vertical muons detected by a plastic scintillator telescope, the first measurement of cosmic-ray flux was $(2.0 \pm 0.4) \times 10^{-10}$ cm^{-2}s^{-1} and had no angular correction to the detector acceptance [10]. Reference [11] categorized underground laboratories into two types: below mountains (mountain shape overburden) and down mine shafts (flat overburden). However, as Ref. [12] pointed out, the flux magnitude is quite different in laboratories situated under mountains and down mine shafts with the same vertical rock overburden. This difference can lead to different background

levels for a variety of physics implications, such as the cosmogenic ^{11}C background in searches for Carbon-Oxygen-Nitrogen solar neutrinos [13], and the cosmic-ray spallation background in searches for the upturn of the solar ^{8}B neutrino spectrum [14] and supernova relic neutrinos [15]. Therefore, a precise total flux measurement and a detailed cosmic-ray leakage study are necessary for the active and passive shielding design of future neutrino experiments.

A 1-ton scintillator detector serves as a prototype of the Jinping Neutrino Experiment and has been running since 2017 [16]. This prototype aims to test the performance of several related key detector components, understand the neutrino detection technology, and measure the underground background level in situ. This study used this omnidirectional detector to measure the cosmic-ray muon flux at CJPL-I, including the muon angular distributions, enabling a clear understanding of the cosmic-ray leakage through the mountain topography profile.

After detailing the design of the 1-ton prototype detector, we describe the model for predicting the underground muon energy and angular distributions, muon event selection, and direction reconstruction. The muon flux measurement based on the two-year data of the 1-ton prototype is then reported.

II.   THE 1-TON PROTOTYPE DETECTOR

Figure 1 shows a schematic diagram of the detector structure. To reduce the environmental background, 20 cm×10 cm×5 cm lead bricks were used to form a shielding wall outside the tank (not drawn in the figure). The detector measures 2 m in height and contains one ton of custom liquid scintillator in a 0.645 m-radius acrylic spherical vessel [16]. This scintillator, referred to as the slow liquid scintillator [17, 18], is a linear alkylbenzene (LAB) doped with 0.07 g/l of the fluor 2,5-diphenyloxazole (PPO) and 13 mg/l of the wavelength shifter 1,4-bis (2-methylstyryl)-benzene (bis-MSB). This slow scintillator delays the scintillation light emission duration
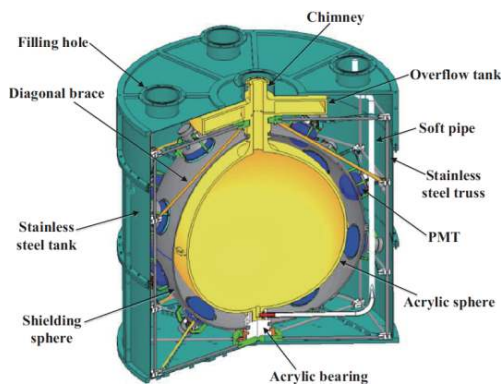
and thus enhances the Cherenkov-to-scintillation light ratio in the early arrival time, to separate these two lights with high efficacy. Thirty 8-inch Hamamatsu R5912 photomultiplier tubes (PMTs) outside the acrylic vessel detect the Cherenkov and scintillation light and output their pulse shapes to front-end electronics. A water buffer layer between the outer layer of the acrylic vessel and the inner wall of the stainless steel tank serves as a passive shielding material to suppress the ambient radioactive background.

The front-end electronics system includes 4 CAEN V1751 FlashADC boards and one logical trigger module CAEN V1495. Each FlashADC board has eight channels, with 10 bit ADC precision for 1 V dynamic range, and a 1 GHz sampling rate. All the PMT signals go directly into the V1751 boards for digitization. If more than 25 PMTs fired, the data acquisition system records all the pulse shapes from the fired PMTs in a 1029-ns time window.

III.   PREDICTED MUON ENERGY SPECTRUM
AND ANGULAR DISTRIBUTION

The energy spectrum and angular distribution of underground muons were used as the inputs for the detector simulation. The muon direction is defined throughout this paper as the direction from which it comes. A Geant4 [19, 20]-based package simulated muon penetration development in the mountain rock to predict various underground muon characteristic profiles, with its own standard electromagnetic and muon-nucleus processes.

Jinping mountain is about 4000 m above sea level, and the elevation of the experiment hall is about 1600 m. We obtained the mountain terrain data from the NASA SRTM3 dataset [21]. Figure 2 shows the contour map. There were 6315 survey points within a 9 km radius
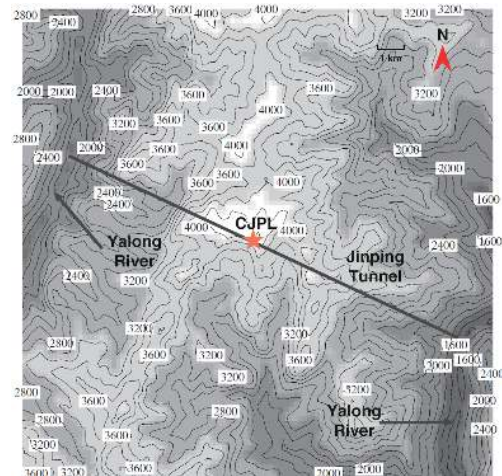

Fig. 1.   (color online) 1-ton prototype of Jinping Neutrino Experiment.

Fig. 2.   (color online) Contour map near CJPL-I, as given by the SRTM3 dataset [21].

circle centered at the laboratory. We assembled them to a mesh using Delaunay triangulation, a standard algorithm, to divide discrete points into a set of triangles with the restriction that two adjacent triangles entirely share each triangle side.

We assume Jinping mountain's average rock density to be 2.8 g/cm^3, from Ref. [10], so the water equivalent depth is 6720 m for 2400 m rock. The density variation can affect the simulated spectrum. However, it is negligible for the flux measurement since, in our case, the detection efficiency is not sensitive to the spectrum, as discussed in Sec. VI.C. The composition of the rock in the simulation utilized the values from the abundance of elements in Earth's crust (percentage by weight) [22]: oxygen (46.1%), silicon (28.2%), aluminum (8.2%), and iron (5.6%). The modified Gaisser's formula [23] parametrizes the kinetic energy E and zenith angle θ distribution of cosmic-ray muons at sea level as

$$G(E,\theta) \equiv \frac{\mathrm{d}N}{\mathrm{d}E\mathrm{d}\Omega} = \frac{I_0}{\mathrm{cm}^2 \cdot \mathrm{s} \cdot \mathrm{sr} \cdot \mathrm{GeV}}$$

$$\times \left(\frac{E^\star}{\mathrm{GeV}}\right)^{-\gamma} \cdot \left(\frac{1}{1 + \dfrac{1.1E\cos\theta^\star}{115\,\mathrm{GeV}}} + \frac{0.054}{1 + \dfrac{1.1E\cos\theta^\star}{850\,\mathrm{GeV}}}\right), \quad (1)$$

where $E^\star$ and $\cos\theta^\star$ are defined as follows:

$$E^\star = E\left[1 + \frac{3.64\,\mathrm{GeV}}{E \cdot (\cos\theta^\star)^{1.29}}\right],$$

$$\cos\theta^\star = \sqrt{\frac{\cos^2\theta + P_1^2 + P_2(\cos\theta)^{P_3} + P_4(\cos\theta)^{P_5}}{1 + P_1^2 + P_2 + P_4}}, \quad (2)$$

where I_0 is a normalization constant, $\gamma = 2.7$ is the muon spectral index, and P_1, P_2, P_3, P_4, and P_5 are the parameters in Ref. [23].

Figures 3 and 4 show the simulated underground muon kinetic energy and corresponding angular distributions at CJPL-I. The uncertainties come from the precision of the NASA dataset (90 m in horizon directions) and the experiment hall size of ∼ 100 m. We also plot the distributions at sea-level for comparison. The expected corresponding zenith angle follows a $\cos^2\theta$ distribution and the azimuth angle follows a uniform distribution. The observed cosmic-ray leak in the southern direction agrees with Fig. 2, in which the contour plot indicates less rock coverage.

Due to the high elevation (∼4000 m), the altitude and latitude may affect the muon distributions described in Eq. (1). However, Ref. [24] pointed out that the differential flux at high energy (> 40 GeV) and small zenith angle barely depends on altitude and latitude. Since the minim-
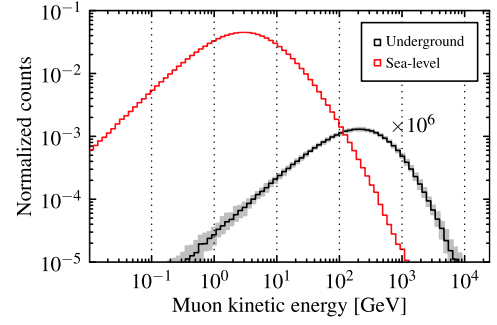

Fig. 3. (color online) Simulation result of underground muon kinetic energy. The mean value is 340 GeV. The gray band shows the 1σ uncertainty. See more details in the text. The spectrum of muons at sea-level is also plotted.
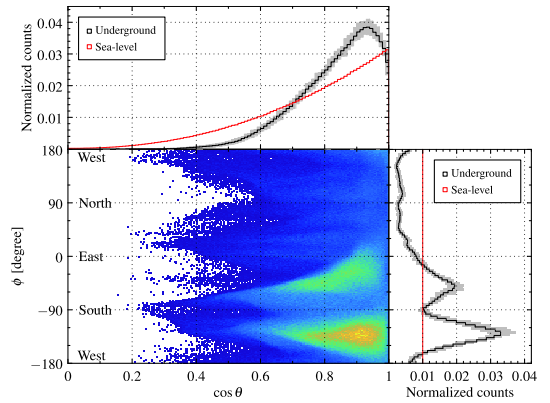

Fig. 4. (color online) Simulation result of underground muon direction ($\cos\theta, \phi$) and one-dimensional projections. Muons from the south are more intense, as expected from the contour map in Fig. 2. The gray band shows the 1σ uncertainty. See more details in the text. The spectrum of muons at sea-level is also plotted.

um energy required for muons to reach CJPL-I is approximately 3 TeV, and the cosine of the zenith angle is concentrated above 0.4, we conclude that CJPL-I's altitude and latitude do not affect the underground muon spectrum.

IV. EVENT SELECTION

This study analyzed the data collected from July 31, 2017 to July 12, 2019. We first required that runs should be flagged as good runs, i.e., neither pedestal calibration nor detector maintenance. Data quality check parameters for identifying apparent noise were the trigger rate, baseline, and baseline fluctuation of a waveform. A data file should not have these quantities deviate from the reference values by more than three standard deviations. The live time after the data quality check was 5.575×10^7 s, or 645.2 live days.

We then required a minimum number of photoelectrons (PEs), corresponding to approximately 100 MeV

energy deposits or 50 cm track length in the scintillator. When passing through the detector's edge, a muon deposits less energy and is indistinguishable from that from the radioactive background, muon showers, or noise events. Therefore, this cut discarded low-energy events to get a high purity sample.

We finally removed the electronics noise and flasher events, which are highly-charged light-emitting events, possibly from discharge of the PMT bases. Examining all the high energy deposit event waveforms, we found that some of them always had a single PMT with a much higher charge than the others, while a muon event was of a more uniform charge distribution. To identify the flasher events, we required that the ratio of maximum PE number of each PMT to total PE number in one event, denoted by $r_{\max}$, should not be greater than 0.15 to identify the flasher events.

Figure 5 shows a two-dimensional distribution and one-dimensional projections of PE number and $r_{\max}$, indicating that the flasher events and the electronic noise events correspond to the clusters with larger $r_{\max}$. We
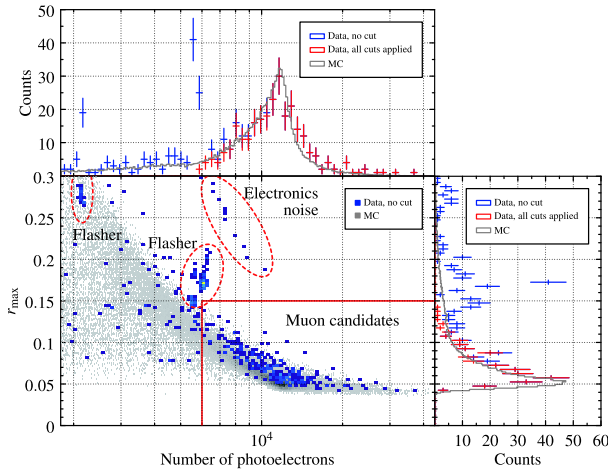

Fig. 5. (color online) Scatter plot and one-dimensional projections of $r_{\max}$ and PE number distribution from the data. The grey area in the two-dimensional distribution is the simulation result. Typical muon candidates spread in the region of $r_{\max} < 0.15$ and PE number > 6000, while flasher and electronics noise events have larger $r_{\max}$ and are distributed in the clusters marked with circles. Low-energy events (PE number < 6000) which may contain indistinguishable radioactive background, shower, or noise events are also removed.

Table 1. Summary of cuts for muon candidate selection.

Type	Selection criteria
Data quality check	Good run
	Trigger rate, baseline and baseline fluctuation
Muon candidate selection	Number of photoelectrons > 6000
	$r_{\max} < 0.15$

also show the simulation result and one-dimensional projections for better comparison. In the end, 264 muon candidates passed the selection criteria. Table 1 summarizes all the selection criteria for muon candidate selection.

V. DIRECTION RECONSTRUCTION

We used a template-based method to reconstruct the muon direction. The templates were generated from a Geant4-based simulation. Each template was tagged with the muon direction $\boldsymbol{p}_i = (\cos\theta, \phi)$ and the entry point on the acrylic vessel $(\cos\alpha, \beta)$, as shown in Fig. 6. When a muon's direction was sampled from a uniform distribution, its entry point on the vessel surface was also sampled uniformly on the hemisphere facing the muon direction.

About 250k template events passed the event selection criteria described in Section 4. For the PMT arrival time pattern vector of template i: $\boldsymbol{T}_i = (t_{0i}, t_{1i}, \cdots, t_{29i})$, we subtracted the mean value $\bar{t}_i = \dfrac{1}{30}\sum\limits_{j=0}^{29} t_{ji}$ for zero centering,

$$\tilde{\boldsymbol{T}}_i = (\tilde{t}_{0i}, \tilde{t}_{1i}, \cdots, \tilde{t}_{29i}) = (t_{0i} - \bar{t}_i, t_{1i} - \bar{t}_i, \cdots, t_{29i} - \bar{t}_i). \quad (3)$$

The zero-centered PMT arrival time pattern vector for data is

$$\tilde{\boldsymbol{T}} = (\tilde{t}_0, \tilde{t}_1, \cdots, \tilde{t}_{29}) = (t_0 - \bar{t}, t_1 - \bar{t}, \cdots, t_{29} - \bar{t}), \quad (4)$$

where $\bar{t} = \dfrac{1}{30}\sum\limits_{j=0}^{29} t_j$. We constructed the corresponding Euclidean distance,
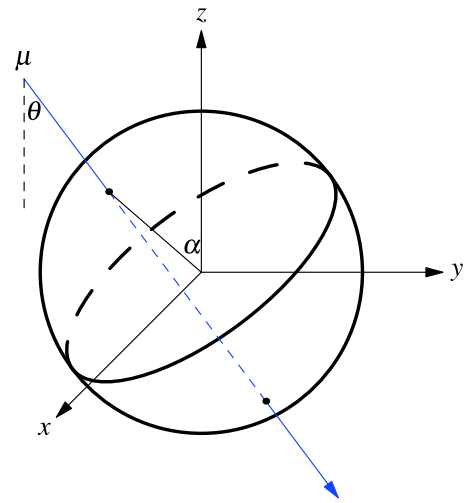

Fig. 6. (color online) Muon generator in the PMT trigger time pattern template. The muon direction $(\cos\theta, \phi)$ and entry point $(\cos\alpha, \beta)$ were sampled uniformly.

$$d_i = |\tilde{\boldsymbol{T}}_i - \tilde{\boldsymbol{T}}| = \sqrt{\sum_{j=0}^{29} \left(\tilde{t}_{ji} - \tilde{t}_j\right)^2}. \tag{5}$$

Then we searched for the k nearest neighbors, where the hyper-parameter k is an arbitrary integer to be chosen later. The reconstructed muon direction $\boldsymbol{P}$ was calculated by the weighted average of the k nearest neighbors,

$$\boldsymbol{P} = \frac{\sum_{i=1}^{k} \dfrac{1}{d_i} \boldsymbol{p}_i}{\sum_{i=1}^{k} \dfrac{1}{d_i}}. \tag{6}$$

We generated a test sample (also uniform muons) to evaluate the reconstruction method performance and determine the hyper-parameter k. The smearing induced by the detector response was included in the test sample to simulate the uncertainty from the electronics hardware and the time calibration. Figure 7 shows that the average included angle between the truth and the reconstructed directions $\Delta\Theta$ varies with the hyper-parameter k and becomes stable at $k = 50$ and above. Therefore, we chose $k = 50$ for the reconstruction. Figure 8 shows that the included angle distribution has a peak value of 10 degrees
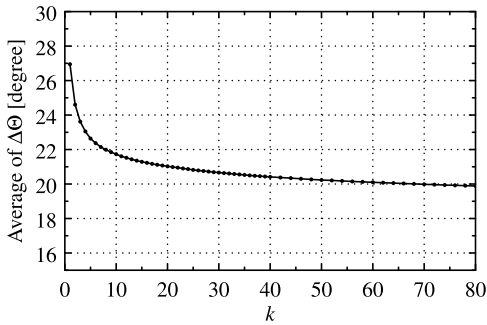

Fig. 9. (color online) Reconstructed $\cos\theta$ and ϕ for the selected muon candidates. Also plotted are the one-dimensional projections for these two angles for the data (black) and the simulation (red).

and an average of 20 degrees. The long tail is due to the limited time resolution of the electronics hardware and PMTs.

Figure 9 shows the $\cos\theta$ and ϕ distributions for both the data and the simulation. Both are consistent. The uneven structure observed for the ϕ distribution indicates the different cosmic-ray leakage due to the mountain structure above CJPL-I.

VI. MUON FLUX MEASUREMENT

A. Detection efficiency

We define the overall efficiency ϵ as the ratio of the number of selected muon candidates N_μ over the total number of muons going through the experiment hall N_{total},

$$\epsilon \equiv \frac{N_\mu}{N_{\text{total}}}. \tag{7}$$

The selected muon candidates contain a small fraction of the muon shower events, due to muon interactions with the atoms of the rock. As a consequence, the incident particles are the parent muons. We had to evaluate this effect in the detection efficiency, so we simulated the whole experiment hall. With the underground muon energy spectrum and angular distribution in Section III, we performed another Geant4-based simulation to study the detection efficiency. Considering the effect of muon showers in the rock and detector components, we added 1 m thick rock in the geometry and generated muons flying towards the five surfaces (excluding the bottom surface) of an 8 m×6 m×5 m experiment hall, as shown in Fig. 10. After being decomposed into a geometry factor ϵ_g, a

Fig. 7. Average included angle $\Delta\Theta$ between the truth and reconstructed directions as a function of the hyper-parameter k.
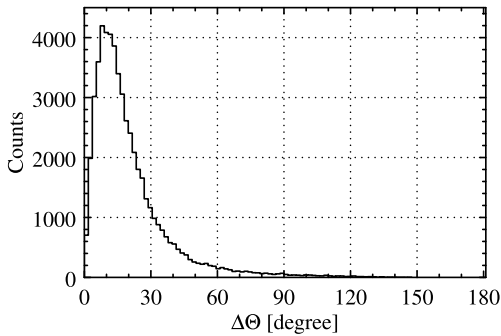

Fig. 8. Included angle $\Delta\Theta$ between the truth and the reconstructed directions for $k = 50$.
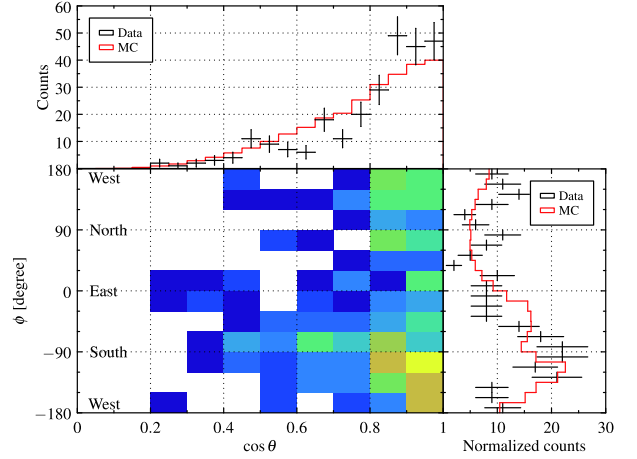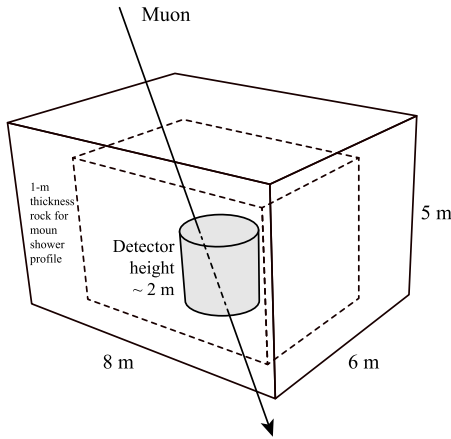
Fig. 10.   Geometry setup in the simulation.

Fig. 11.   (color online) Projection area (gray) of the surface (α, β) for the muon direction (θ, ϕ).

detection efficiency ϵ_d, and a shower factor ϵ_s, the overall efficiency becomes

$$\epsilon = \epsilon_g \cdot \epsilon_d + \epsilon_s, \tag{8}$$

$$\epsilon_g = \frac{N_p}{N_{\text{total}}}, \quad \epsilon_d = \frac{N_1}{N_p}, \quad \epsilon_s = \frac{N_2}{N_{\text{total}}}, \tag{9}$$

where N_p is the number of muons passing through the scintillator target, N_1 is the number of detected muons passing through the scintillator target, and N_2 is the number of detected muon shower events, $N_\mu = N_1 + N_2$. The simulation results show that

$$\epsilon = 1.70\%, \ \epsilon_g = 2.02\%, \ \epsilon_d = 82.7\%, \ \epsilon_s = 0.04\%. \tag{10}$$

The detection efficiency $\epsilon_d = 82.7\%$ indicates that the efficiency loss in the event selection is less than 20%.

As shown in Fig. 11, for a surface S with normal direction $(\alpha_{\text{zenith}}, \beta_{\text{azimuth}})$ and muon direction (θ, ϕ), the horizontal projection area S_{p} is given by

$$S_{\text{p}}(\theta, \phi) = |\sin\alpha \tan\theta \cos(\beta - \phi) + \cos\alpha| S. \tag{11}$$

We define S_i as the projection area of the i-th surface, which is an integral for the normalized incoming muon spectrum $f(E_k, \theta, \phi)$ obtained from the simulation result of Section III,

$$S_i = \int S_{\text{p}}(\theta, \phi) f(E_k, \theta, \phi) \, \mathrm{d}(\cos\theta) \mathrm{d}\phi. \tag{12}$$

The experiment hall projection area S_{total} is the sum of the five surfaces,

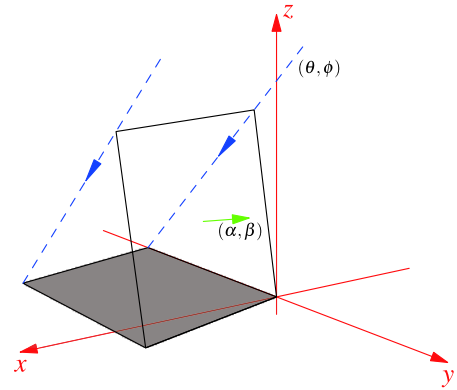$$S_{\text{total}} = \sum_{i=1}^{5} S_i = 78.7 \, \text{m}^2. \tag{13}$$

B. Muon flux result

The muon flux ϕ_μ was calculated by

$$\phi_\mu = \frac{N_{\text{total}}}{T \cdot S_{\text{total}}} = \frac{N_\mu / \epsilon}{T \cdot S_{\text{total}}}, \tag{14}$$

where T is the live time and N_μ is the number of muon candidates. By defining $S \equiv \epsilon S_{\text{total}}$ as the active area, we simplified the 1-ton prototype detector flux calculation to

$$\phi_\mu = \frac{N_\mu}{T \cdot S} = 3.53 \times 10^{-10} \, \text{cm}^{-2} \text{s}^{-1}. \tag{15}$$

The simulation results show that the active area $S = 1.34 \ \text{m}^2$ is close to the cross-section of the liquid scintillator sphere of the detector, which is $1.31 \ \text{m}^2$.

C. Systematic uncertainties

Table 2 summarizes the systematic uncertainties, which mainly come from two components: (1) the PE number calculation (energy scale) in the data and (2) the efficiency calculation in the Monte-Carlo simulation. A quadrature sum of the individual components gives the total systematic uncertainty.

The conversion from the charge to the number of PEs was done through a PMT gain factor. A run-by-run PMT calibration corrected the gain drift and introduced a 2.0% systematic uncertainty for the 6,000 p.e. cut, corresponding to a 0.6% efficiency variation in flux measurement.

The uncertainty in the efficiency calculation comes from the parameters in the simulation inputs. We compared the data and simulation PE distribution and tuned the scintillation light yield to ensure consistency between the data and simulation. The systematic uncertainty for the consistency was obtained from the Pearson's χ^2,

$$\chi^2 = \sum_{i=1}^{\text{nbins}} \frac{(n_i^{\text{data}} - n_i^{\text{sim}})^2}{n_i^{\text{data}}}, \tag{16}$$

Table 2. Summary of uncertainties for the muon flux measurement.

Source	Parameter uncertainty	Flux measurement uncertainty
Energy scale	±2.0%	±0.6%
Efficiency calculation		
PE yield	±1.6%	±0.5%
Acrylic vessel radius	±0.5 cm	±1.6%
Lead shielding thickness	±5 cm	±0.6%*
Rock thickness for muon shower profile	±50 cm	±0.8%*
Muon spectra	–	±0.7%*
Total systematic	–	±2.2%
Statistical	–	±6.2%

* Dominated by the statistical uncertainty of the Monte Carlo process.

where n_i^{data} is the count in the i-th bin for the data distribution, and n_i^{sim} is the count in the i-th bin for the simulation distribution. The systematic uncertainty of PE yield in the simulation was set to the variation at $\chi_{\min}^2 + 1$.

The acrylic vessel is formed of two hemispheres glued together, for which the machining accuracy was estimated to 5 mm according to the international tolerance grade. This contributed a 1.6% systematic uncertainty in the efficiency calculation.

The muon showers in the rock and lead shielding also contributed to the global efficiency. We placed 1 m depth of rock in the simulation. To verify whether that depth is enough, we added or subtracted 0.5 m rock in different simulations to observe the variation and found that the global efficiency was not sensitive to rock depth. The lead wall thickness was not uniform due to different arrangements of the lead bricks. We changed the thickness by ±5 cm, the typical size of a lead brick, in the simulations, and found little variation in the global efficiency. Limited by the statistical uncertainty of Monte-Carlo, the above studies gave 0.6% and 0.8% systematic uncertainty for the muon shower effect.

We scanned different muon spectra (energy and angular distribution) in Section III in the detection efficiency simulation. Thanks to the detector's spherical symmetry, the uncertainty from the muon spectra was also small and dominated by the statistical uncertainty of the Monte Carlo process.

D. Discussion

The monthly average muon candidate rate appears constant in Fig. 12. The seasonal modulation of muon flux is unobservable because the statistical uncertainty is much larger than the seasonal variation ($\sim 1.3\%$ in Ref. [25]). The total measured cosmic-ray muon flux is $(3.53 \pm 0.22_{\text{stat.}} \pm 0.07_{\text{sys.}}) \times 10^{-10}$ cm^{-2}s^{-1}. The vertical intensity I is calculated to be $(2.0 \pm 0.3_{\text{stat.}}) \times 10^{-10}$ cm^{-2}s^{-1}sr^{-1} using the 47 muon candidates (N_I) reconstructed in $0.95 < \cos\theta < 1$,

$$I = \frac{N_I}{T \cdot S \cdot \Omega}, \qquad (17)$$

where T and S are the live time and active area described in Sec. VI.B, and $\Omega = 0.314$ is the solid angle for $0.95 < \cos\theta < 1$. We also studied the flux variation as a function of horizontal location at CJPL-I using a Geant4-based simulation. The result indicated that the variation should be less than 2.3% along the east-west direction within a variation of 100 m.

Figure 13(a) shows the vertical intensity of muons at WIPP [26], Soudan [27], Boulby [28], Sudbury [29], Kamioka [30], Gran Sasso [25], Fréjus [31], and Jinping as a function of vertical overburden. Also plotted is the prediction by a parametrized formula, given by Ref. [12],

$$I(h) = I_1 e^{-h/\lambda_1} + I_2 e^{-h/\lambda_2} \qquad (18)$$

where $I(h)$ is the differential muon intensity corresponding to the slant depth h, and $I_1, I_2, \lambda_1, \lambda_2$ are parameters in Ref. [12]. The measurement result in this work is consistent with Eq. (18).

Figure 13(b) summarizes the total muon flux measured at different underground sites. WIPP, Soudan,
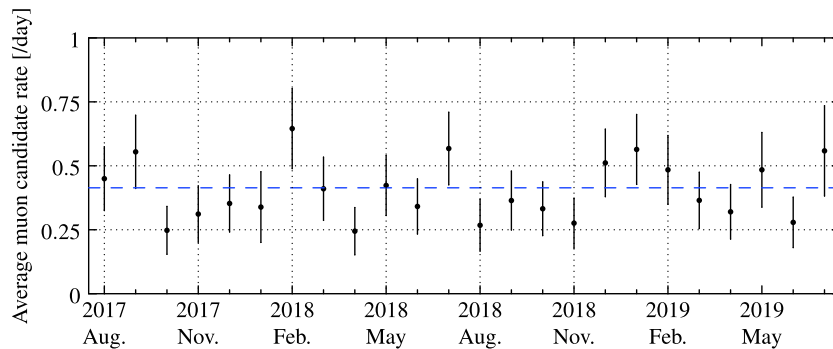
Fig. 12. (color online) Cosmic-ray muon rate measured by the 1-ton prototype at CJPL-I, as a function of time. The data are shown in monthly bins.
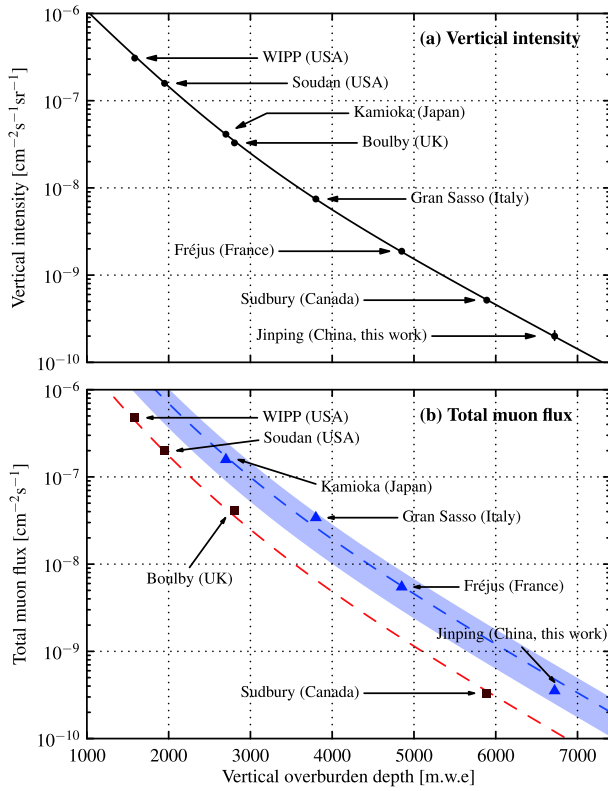
Fig. 13. (color online) Measurements of the vertical intensity (a) and total muon flux (b) at different underground sites. The red dashed line in (b) is the empirical formula for the mine shaft case. The blue dashed line and shaded area in (b) are the fitting result and uncertainty respectively for the factor F.

Boulby, and Sudbury are labs situated down mine shafts, while Kamioka, Gran Sasso, Fréjus, and Jinping are below mountains. The underground muon flux ϕ is a complicated integral over the muon spectrum $f(E_k, \theta, \phi)$ and slant depth (or muon track length) d,

$$\phi = \int f(E_k, \theta, \phi) \cdot p(E_k, d) \, \mathrm{d}E_k \mathrm{d}\theta \mathrm{d}\phi, \qquad (19)$$

where $p(E_k, d)$ is the survival probability at slant depth d. For the mine shaft (flat overburden) case, we have $d = h/\cos\theta$. We simulated the muon flux at 50 different depths for the flat overburden case, using Geant4. For simplicity, we fitted these simulation points with a series expansion of Eq. (19),

$$\phi_0(h) = \exp\left(a_0 + a_1 h + a_2 h^2 + a_3 h^3 + a_4 h^4\right) \mathrm{cm}^{-2}\mathrm{s}^{-1}, \quad (20)$$

where $\phi_0(h)$ is the muon flux at vertical overburden depths h (in km.w.e), $a_0 = -10.147$, $a_1 = -3.385\,\mathrm{km}^{-1}$, $a_2 = 0.404\,\mathrm{km}^{-2}$, $a_3 = -0.0344\,\mathrm{km}^{-3}$, $a_4 = 0.00111\,\mathrm{km}^{-4}$. The differences between the empirical formula and data are -6.9% (WIPP), -2.6% (Soudan), -13.3% (Boulby), and 5.7% (Sudbury). The red dashed line in Fig. 13(b) plots the fitting result.

The total muon flux of a lab situated below a mountain, $\phi_1(h)$, can be scaled by a factor F to $\phi_0(h)$,

$$\phi_1(h) = F \cdot \phi_0(h). \qquad (21)$$

Usually $F > 1$ because the mountain case has less rock shielding, which leads to a more considerable muon flux. The factors F were 3.7 (Kamioka), 5.2 (Gran Sasso), 3.9 (Fréjus) and 2.9 (Jinping). We assumed that mountains on the Earth have similar topography and elemental compositions so that the factors for different locations would not vary too much. We fitted these four labs using the empirical formula in Eq. (21) with an uncertainty assigned so that χ^2/ndf is one. The fitting result $F = (4.0 \pm 1.9)$ and this uncertainty account for the variation of mountain topography profiles. The blue dashed line in Fig. 13(b) illustrates the fitting result. Using ϕ_0 and factor F, anyone can easily get a rough estimate from the vertical overburden without doing any simulation or measurement.

VII. SUMMARY

We studied the cosmic-ray muons at CJPL-I using the 1-ton prototype of the Jinping Neutrino Experiment. This study determined the muon flux to be $(3.53 \pm 0.22_{\mathrm{stat.}} \pm 0.07_{\mathrm{sys.}}) \times 10^{-10} \ \mathrm{cm}^{-2}\mathrm{s}^{-1}$. The zenith and azimuth angle distributions show that cosmic-ray leakage is due to the mountain topography profile, as expected. A survey of muon fluxes at different laboratories situated under mountains and down mine shafts indicated that the flux at the former is generally a factor of (4.0 ± 1.9) larger than at the latter, for the same vertical overburden. This study provides a reference for passive and active shielding designs for future underground neutrino experiments.

References

[1]   J. Cheng *et al.*, Annual Review of Nuclear and Particle Science **67**, 231-251 (2017)

[2]   K. Kang *et al.*, *Status and prospects of a deep underground laboratory in china*, in: Journal of Physics: Conference Series, Vol. 203, IOP Publishing, 2010, p. 012028

[3]   Q. Yue *et al.*, Phys. Rev. D **90**, 091701 (2014)

[4]   M. Xiao *et al*., *First dark matter search results from the PandaX-I experiment*, Science China Physics, Mechanics and Astronomy **57**, 2024–2030 (2014)

[5]   L. Wang *et al*., *First results on 76Ge neutrinoless double beta decay from CDEX-1 experiment*, Science China Physics, Mechanics and Astronomy **60**(7), 071011(2017)

[6]   X. Chen *et al*., Sci. China Phys. Mech. Astron. **60**(6), 061011 (2017)

[7]   J. F. Beacom *et al*., Chinese Physics C **41**(2), 023002 (2017)

[8]   L. Wan *et al*., Phys. Rev. D **95**, 053001 (2017)

[9]   O. Šrámek *et al*., Phys. Rev. D **6**, 33034 (2016)

[10]   Y. Wu *et al*., Chinese Physics C **37**(8), 086001 (2013)

[11]   L. Mayor, Physics World **28**(5), 28-28 (2015)

[12]   D. Mei and A. Hime, Phys. Rev. D **73**, 053004 (2006)

[13]   M. Agostini *et al*., *Sensitivity to neutrinos from the solar CNO cycle in Borexino* (2020), arXiv: 2005.12829

[14]   K. Abe *et al*., Phys. Rev. D **94**, 052010 (2016)

[15]   Y. Zhang *et al*., Phys. Rev. D **93**, 012004 (2016)

[16]   Z. Wang *et al*., Nucl. Instrum. Methods A **855**, 81-87 (2017)

[17]   M. Li *et al*., Nucl. Instrum. Methods A **830**, 303-308 (2016)

[18]   Z. Guo *et al*., Astropart. Phys. **109**, 33-40 (2019)

[19]   S. Agostinelli *et al*., Nucl. Instrum. Methods A **506**(3), 250-303 (2003)

[20]   J. Allison *et al*., IEEE Transactions on Nuclear Science **53**, 270-278 (2006)

[21]   T. G. Farr *et al*., *The shuttle radar topography mission*, Reviews of Geophysics 45 (2007)

[22]   D. R. Lide, *CRC handbook of chemistry and physics*, Vol. 97, CRC press, 2016

[23]   M. Guan *et al*., *A parametrization of the cosmic-ray muon flux at sea-level* (2015), arXiv: 1509.06176

[24]   S. Cecchini and M. Sioli, *Cosmic ray muon physics, in: Non-accelerator particle astrophysics,* Proceedings, 5th ICTP School, 1998, pp. 201–217

[25]   G. Bellini *et al*., Journal of Cosmology and Astroparticle Physics **05**, 015 (2012)

[26]   E.-I. Esch *et al*., Nucl. Instrum. Methods A **538**(1-3), 516-525 (2005)

[27]   S. Kamat, *Extending the sensitivity to the detection of WIMP dark matter with an improved understanding of the limiting neutron backgrounds*, Ph.D. thesis, Case Western Reserve University (2005)

[28]   M. Robinson *et al*., Nucl. Instrum. Methods A **511**(3), 347-353 (2003)

[29]   B. Aharmim *et al*., Phys. Rev. D **80**, 012001 (2009)

[30]   K. Eguchi *et al*., Phys. Rev. Lett. **90**, 021802 (2003)

[31]   C. Berger *et al*., Phys. Rev. D **40**, 2163-2171 (1989)